PHOTONICS Research

Theoretical and practical guide for an axial superresolved focus via Gouy phase steering

Xiaowei Liu,[1,2,4] Xiaolan Xia,[1] Zhuofan Yao,[1] Tianyue Zhang,[1] Meiling Jiang,[1] Qing Yang,[2,3] Xiangping Li,[1] and Yaoyu Cao[1,5]

[1]*Guangdong Provincial Key Laboratory of Optical Fiber Sensing and Communications, Institute of Photonics Technology, Jinan University, Guangzhou 510632, China*
[2]*Research Center for Humanoid Sensing, Zhejiang Lab, Hangzhou 311121, China*
[3]*State Key Laboratory of Modern Optical Instrumentation, College of Optical Science and Engineering; International Research Center for Advanced Photonics, Zhejiang University, Hangzhou 311121, China*
[4]*e-mail: liuxiaowei@zhejianglab.com*
[5]*e-mail: yaoyucao@jnu.edu.cn*

Achieving an axial superresolved focus with a single lens by simply inserting a modulation mask in the pupil plane is preferred due to its compact configuration and general applicability. However, lack of a universal theoretical model to manifest the superresolved focusing mechanism vastly complicates the mask design and hinders optimal resolution. Here we establish an interference model and find out that the axial resolution closely relates to the Gouy phase gradient (GPG) at the focal point. Using a GPG tuning-based optimization approach, the axial resolution of a ring-mask-modulated beam is readily improved to attain superresolved focal depth for multiple types of pupil function and polarization. In experiment, a focus with an axial resolution of 27% improved from the diffraction limit and 11% finer than the previously reported record is demonstrated for the radially polarized beam. In simulations, a spherical focus with 3D isotropic resolution and a superoscillation-like axial modulation behavior toward extremely high axial resolution is also presented. This approach can be applied for varied types of pupil function, wavelength, and polarization, and can be easily transferred to other traditional or superresolution microscopes to upgrade their axial resolution. © 2022 Chinese Laser Press

https://doi.org/10.1364/PRJ.467976

1. INTRODUCTION

Isotropic resolution is progressively desirable in laser fabrication and microscopy imaging [1–15], while unfortunately, conventional focal region is inherently of anisotropic configuration subjected to optical lens design and the diffraction nature of light. For example, a plane wave is commonly transformed into an elliptical focal spot, with its axial size more than 2 times its lateral size, after a lens. Tremendous attention has been paid to increase the axial resolution in recent decades. The total internal reflection fluorescence microscopy uses evanescent wave illumination and provides high-contrast axial superresolution image of a thin layer of object within the evanescent wave penetration depth. In the case of acquiring a larger axial field of view, 3D scanning methods with a compressed point spread function are dominating currently, including stimulated emission depletion (STED) microscopy, two-photon/multi-photon microscopy, confocal microscopy, 4π technique, and the simultaneous spatial temporal focusing approach [16–24]. Implementations of these methods rely on their unique optical configurations. STED incorporates two parallel laser beams in illumination, one of which is modulated by a vortex phase plate

so as to form a hollow focus to deactivate the fluorescent signal generated by the other beam. Confocal configuration blocks the signal out of focus by placing a pinhole in the conjugate position of the illumination focus. 4π technique utilizes two well aligned head-to-head objectives, which is particularly suited to transparent and thin samples. The simultaneous spatial temporal focusing approach uses a chromatically dispersed femtosecond laser in illumination.

In practice, an axial superresolution method with compact configuration, extraordinary compatibility, and flexibility that can be easily transferred to the other microscope systems to enable a better performance, is immensely preferred. Beam modulation by directly inserting a mask in the pupil plane to squeeze the focal spot axially possesses the features above. Different kinds of modulation masks have been reported [25–28], including the binary phase-only mask and the annular amplitude mask. These pupil masks, demonstrated previously, were designed either empirically or by search algorithms, as far as we know. The Toraldo concept [28] has established a Fourier transform relationship between the axial amplitude of the focus and the pupil transmittance distribution, which nonlinearly

relates to the pupil radius and thus makes the pupil mask difficult to fabricate in practice. Lack of a universal theoretical model to analyze the pupil modulation-based axial superresolved focusing has largely burdened mask design and hindered achieving the optimal resolution.

In this paper, we analyze the axial superresolved focusing process from an interference perspective and find that the axial resolution closely relates to the gradient of the Gouy phase, which is used to describe the phase anomaly of a focused field with respect to an ideal spherical wave. Based on this finding, we propose an axial interference model and develop a Gouy phase steering method. This method can be universally applied to varied types of incident polarization and objective numerical apertures (NAs) and can be transplanted to optimize multiple kinds of pupil function for axial superresolution. It also shows the potential to attain a superresolved focal length that can even be extremely shortened, similar to the lateral resolution modulation based on superoscillation [29,30]. We use this method to optimize a shaded-ring pupil mask, i.e., a binary amplitude modulation mask. The approach has been implemented on the linearly polarized beam and radially polarized beam, respectively, to achieve the axial superresolution. The results have clearly evidenced its superiority to previous studies on pupil masks designed by experience or by a searching algorithm. We show that both in simulations and experiments, the axial resolution of a radially polarized beam can be 27% enhanced from the diffraction limit and can be 11% finer than the previously reported record without increasing the sidelobe intensity [25]. Additionally, by introducing more rings in the pupil mask based on this method, the energy residing in the sidelobes can be further suppressed and precisely redistributed according to their influence in the specific applications. A spherical focus, with a ratio of 1:1:1.06 between the full widths at half-maximum (FWHMs) in the x, y, and z directions, is also demonstrated in simulation for a radially polarized beam, which evidences the isotropic resolution by using a compact and simple single objective configuration. Finally, by applying the method to design a π phase ring mask, a superoscillation-like behavior can be observed in the axial dimension with the conceptual possibility toward extremely high axial resolution.

2. MECHANISM AND SIMULATIONS

In the axial superresolution method concerning the Gouy phase gradient (GPG), the pupil mask $[P(x,y)]$ is decomposed to a clear pupil (constant distribution of 1) and an inverse mask $[P(x,y) - 1]$. Optimization of the inverse mask $[P(x,y) - 1]$ is equivalent to the optimization of the pupil mask $[P(x,y)]$. Based on the Huygens–Fresnel principle, the final focus can be treated as an interference between the focus formed with the clear pupil (denoted as "clear focus" in the following) and the focus formed with the inverse pupil mask (denoted as "inverse focus" in the following). The completely destructive interference between the clear focus and the inverse focus along the axis can shorten the axial focal depth, which provides a theoretical constraint condition for the parameter optimization in the pupil plane. To demonstrate this interference concept and the mask design mechanism, we mainly take use of a shaded-ring mask model as an example, in which a ring zone

is amplitude-attenuated [25,27,31] [Fig. 1(a)], owing to its usually enabling axially superresolved focus accompanied with sidelobes of low intensity. It should be emphasized that this method does not merely work for the shaded-ring mask design.

For a shaded-ring pupil mask, the inverse pupil mask $[P(x,y) - 1]$ is an amplitude-attenuated, π-phase ring-pass mask [Fig. 1(a)]. Based on the proposed interference model, the parameters, including the ring radius and the amplitude attenuation, can be designed and calculated, rather than using a search algorithm. To graphically show the effect of the interference on axial superresolved focusing, we plot the amplitude and phase distribution of the clear focus and the inverse focus along the z axis [Figs. 1(b) and 1(c)]. Coordinates of the focus center are $x = y = z = 0$. To ensure the completely destructive interference between the clear focus and the inverse focus, phase difference of π and equal amplitude near $z = 0$ should be satisfied simultaneously between the two foci. At the focus center where $z = 0$, the phases of the two foci differ by π [Fig. 1(c)] because the phases at the clear pupil and the inverse
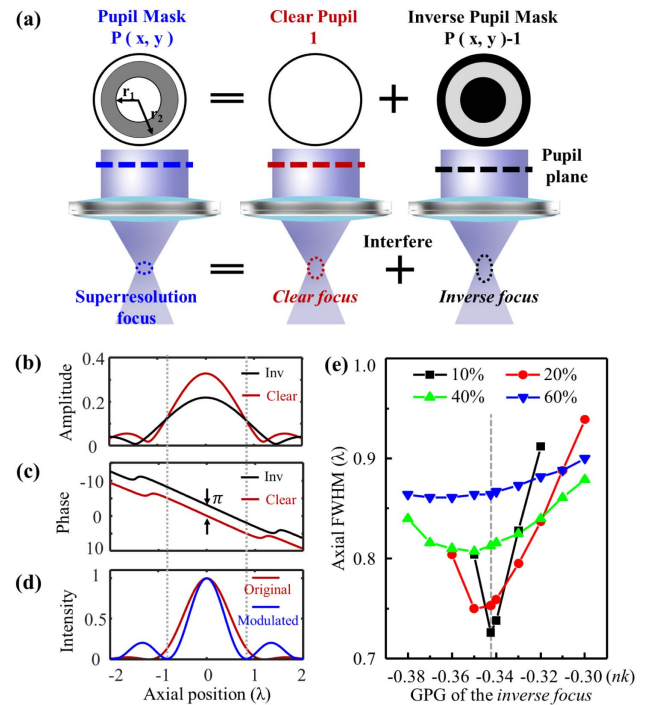

Fig. 1. Schematic diagram of the pupil mask design for axially superresolved focusing based on GPG tuning. (a) Decomposition of a shaded-ring pupil mask $[P(x,y)]$ to a clear pupil and an inverse pupil mask $[P(x,y) - 1]$. The superresolved focus is an interference of the two foci corresponding to the decomposed pupils. (b)–(d) Amplitude and phase distribution of the clear focus and the inverse focus along z axis, and their interfered intensity distribution (blue curve), of a radially polarized beam; gray dashed lines show where the completely destructive interference between the two foci occurs. The normalized inner radius, outer radius [r_1 and r_2 in (a)], and amplitude attenuation of the shaded-ring mask are 0.46, 0.975, and 0.81. The focusing efficiency is 8.11%. (e) The optimal axial resolution of a radially polarized beam focus when the GPG of the inverse focus is tuned to different values. Sidelobe intensity is fixed at 20%. Different color denotes different power transmittance of the shaded-ring mask. The gray dashed line denotes the GPG of the clear focus.

pupil differ by π, and then the light propagates an equal distance from the pupil plane to the focus center. While the amplitude of the clear focus is larger than that of the inverse focus, at a certain distance from the focus center, equal amplitude can be satisfied [shown by gray dotted lines in Fig. 1(b)]. Only if the phases of the two foci still differ by π at that position apart from the focus center, can the completely destructive interference occur. Consequently, the slope of the Gouy phase distribution [see Eq. (1)] along the axis should be the same between the clear focus and the inverse focus, to enable the unchanged phase difference of π [shown in Fig. 1(c)]. We call it the equal Gouy phase gradient (EGPG) condition, which is a necessary condition for the completely destructive interference between the clear focus and the inverse focus to have an axially superresolved focus. Figure 6 in Appendix B shows the simulated microscopy images formed by the clear focus and superresolution focus, respectively, for a clearer demonstration. The EGPG condition is satisfied in Figs. 1(b)–1(d), and a completely destructive interference can be observed at the positions labeled by the two dark dotted lines, leading to a narrower width of the main lobe than the unmodulated focus [Fig. 1(d)]. Inevitably, the focusing efficiency in proportion to the energy residing in the main lobe would be decreased due to the destructive interferences in the main focal area.

Based on this understanding, we proposed a GPG tuning model to design the pupil mask for axial superresolved focusing. The GPG of the inverse focus at $z = 0$ [denoted as $\mathrm{d(GP_{inv})}/\mathrm{d}z|_{z=0}$] can be calculated by Eq. (1). The calculation approach here can be understood as the tilted wave average method. Different from the vectorial-diffraction-theory-based approach to calculate the exact complex amplitude, the phase is analyzed by averaging the phase retardations of the decomposed tilted waves by their normalized amplitude [32] (see Appendix I for the detailed deduction). To conveniently tune the GPG of the inverse focus, we introduce a tool function of the convergence angle, and then the GPG of the inverse focus can be calculated by Eq. (2). The tool function is shown in Eq. (3), whose expression relates to the target value (denoted as $\mathrm{GPG_{target}}$) to which the GPG of the inverse focus is to be tuned,

$$
\left.\frac{\mathrm{d(GP_{inv})}}{\mathrm{d}z}\right|_{z=0} = \int_{\theta_1}^{\theta_2} A(\Theta) \cdot n \cdot k \cdot \cos\Theta \mathrm{d}\Theta
$$
$$
/ \int_{\theta_1}^{\theta_2} A(\Theta)\mathrm{d}\Theta - n \cdot k, \qquad \textbf{(1)}
$$

$$
\left.\frac{\mathrm{d(GP_{inv})}}{\mathrm{d}z}\right|_{z=0} = \frac{T(\theta_1) - T(\theta_2)}{\int_{\theta_1}^{\theta_2} A(\Theta)\mathrm{d}\Theta} + \mathrm{GPG_{target}}, \qquad \textbf{(2)}
$$

$$
T(\theta) = \int_{a\cos\left(\frac{\mathrm{GPG_{target}}+n\cdot k}{n\cdot k}\right)}^{\theta} A(\Theta) \cdot (\mathrm{GPG_{target}} - n\cdot k\cos\Theta + n\cdot k)\mathrm{d}\Theta,
$$
$$
\textbf{(3)}
$$

where $\mathrm{GP_{inv}}$ denotes the Gouy phase of the inverse focus; $\mathrm{GPG_{target}}$ denotes the target value of the GPG of the inverse

focus; n denotes the refractive index of the medium; k denotes the wave vector; and $A(\Theta)$ denotes the amplitude contribution to the focal point at the convergence angle Θ by an incident light beam with uniform intensity distribution.

In order to tune the GPG of the inverse focus to the value of $\mathrm{GPG_{target}}$, $T(\theta_1)$ needs to be equal to $T(\theta_2)$, which ensures $\mathrm{d(GP_{inv})}/\mathrm{d}z = \mathrm{GPG_{target}}$ in Eq. (2). The EGPG condition can be satisfied by making $\mathrm{GPG_{target}} = \mathrm{GPG_{clear}}$, where $\mathrm{GPG_{clear}}$ denotes the GPG of the clear focus.

There are three steps in the GPG tuning-based method to calculate the parameters of a shaded-ring mask.

(1) Calculate pairs of inner and outer radii of the inverse mask, enabling a target GPG of the inverse focus. The convergence angles corresponding to the inner and outer radii of the inverse mask should have the equal T function value [shown in Eqs. (2) and (3)]. Figure 2(a) shows the schematic diagram of the ring-shaped inverse mask. The normalized ring radii (r_1 and r_2) can be calculated from the corresponding convergence angles (θ_1 and θ_2) by $r_i = \sin\theta_i/(\mathrm{NA}/n)$, $i = 1$ or 2.

(2) According to tolerance to the power transmittance, calculate the amplitude transmittance of the shaded-ring mask with different pairs of radii. See Eq. (4),

$$
P = 1 - (1 - A_{\mathrm{tran}}^2)(r_2^2 - r_1^2), \qquad \textbf{(4)}
$$

where P is the power transmittance of the pupil mask; r_1 and r_2 are the normalized inner and outer radii of the shaded ring; and A_{tran} is the amplitude transmittance of the shaded ring.

(3) Calculate the axial sidelobe intensity with varied radii and attenuations and determine the final parameters according to the tolerance to the sidelobe intensity.

When the GPG of the inverse focus is tuned to be equal to the GPG of the clear focus, the completely destructive interference could occur within the Abbe diffraction length, and the minimum axial FWHM tends to appear. The GPG tuning method can be applied to various types of polarization. Here, we take a radially polarized beam as an example to illustrate the influence of the inverse focus GPG on the final axial resolution, as well as to show the mask design process in detail. The axial FWHMs of a radially polarized beam focus with the GPG of the inverse focus tuned at different values are plotted for comparison, as shown in Fig. 1(e). The power transmittance of the shaded-ring mask is set at 10%, 20%, 40%, and 60%, respectively (corresponding to different colors), and the sidelobe tolerance of all the calculated superresolved foci is set as 20%. The data set plotted in each color presents the axial FWHMs with the same power efficiency and sidelobe intensity, but for different GPGs of the inverse focus. When the power transmittance is large, the minimum axial FWHM is achieved with the GPG of the inverse focus vaguely less than the clear focus. In such a case, the axial FWHM changes slightly, which reveals that in a condition with high transmittance, the GPG of the inverse focus equal to the clear focus can give rise to an FWHM rather close to the minimum value. When the power transmittance decreases from 60% to 10%, a smaller axial FWHM can be achieved, and the GPG of the inverse focus that corresponds to the minimum axial FWHM converges to the GPG of the clear focus. It is noteworthy that, in the case of a smaller final focus, which is expected, the distance
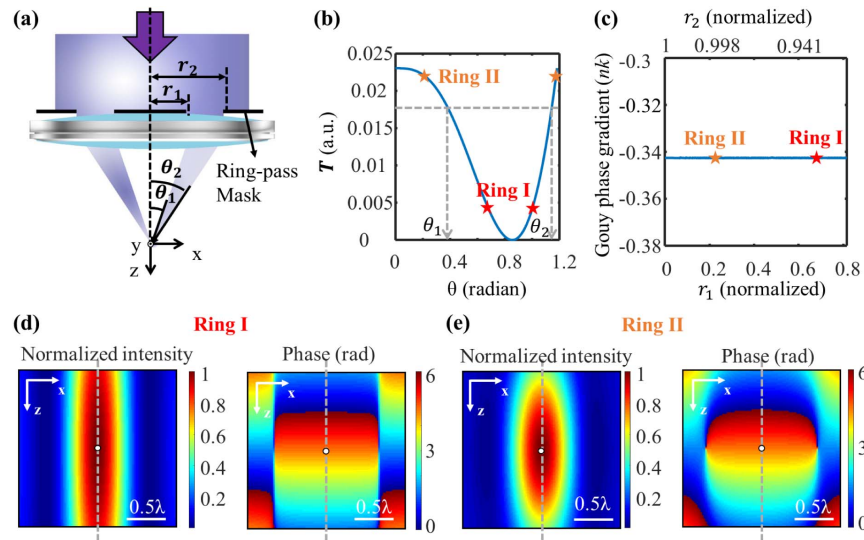
Fig. 2. Calculation of the inner and outer radii of the inverse mask to satisfy EGPG condition. (a) Schematic of the inverse mask for a shaded-ring pupil mask; (b) radius determination tool function; (c) GPG of the inverse focus at focus center, which maintains at GPG of the clear focus, i.e., $-0.3425nk$; (d), (e) focus intensity and phase distribution corresponding to two pairs of inner and outer radii of the ring mask selected in (b), (c) (labeled by red and orange stars, respectively). The white dots and gray dot lines represent the focus center and the optical axis, respectively. Scale bar, half wavelength; NA of the objective, 1.4; $n = 1.514$.

between the two completely destructive interfered points [labeled by gray dotted lines in Figs. 1(b)–1(d)] is closer, and the Gouy phase can be better approximated to a linear distribution; then the EGPG condition should be satisfied more critically as a consequence.

Based on the analysis above, we can tune the inverse focus GPG to the value of the clear focus GPG during the mask design. Figure 2(b) plots the constructed T function value versus the convergence angle, by making $GPG_{target} = GPG_{clear}$ in Eq. (3). The θ_1 and θ_2 should be determined corresponding to the equal T function value, as illustrated by the gray dotted lines. Figure 2(c) shows the GPG of the inverse focus, which is maintained at the GPG of the clear focus with these calculated r_1 and r_2. We randomly select two pairs of inner and outer convergence angles in Figs. 2(b) and 2(c), as shown by "Ring I" and "Ring II" in the figure, and plot the intensity and phase distribution of the focus, as shown in Figs. 2(d) and 2(e). The FWHM of the focus intensity distribution in the axial direction decreases with a wider ring, while the phase distribution on the optical axis changes slightly, and the phase gradient is unchanged at the focal point.

For each pair of θ_1 and θ_2 (or r_1 and r_2), the amplitude attenuation can be correspondingly obtained, given the power transmittance of the mask. Low transmittance of the total pupil can be overcome in practice by increasing the input power. In the meantime, the intensity of sidelobes, which is customarily pursued at a low level in microscope applications, should be more carefully controlled with a sophisticated pupil modulation design. The axial FWHMs and sidelobes of a radially polarized beam focus corresponding to 30% pupil power transmittance are shown in Fig. 3(a). Smaller FWHM comes with higher sidelobe intensity. A 0.75-λ-FWHM can be achieved with 30% sidelobe intensity, as shown in Figs. 3(b) and 3(c) (pupil mask

parameters: $r_1 = 0.479$, $r_2 = 0.972$; and the amplitude attenuation of the ring is 0.855). The focusing efficiency in the modulation is 6.87%. The lateral resolution could be slightly degraded when accompanied with the axial resolution improvement, as shown in Fig. 3(d). The axial FWHM is 27% improved from the 1.03-λ-FWHM of the diffraction-limited focus and 11% finer than the FWHM record of 0.84-λ, with 30% sidelobe reported in the previous simulation work [25].

To achieve a minimized quasi-spherical focus, we further used a lower power transmission (20%) and a higher sidelobe intensity (50%) for the radially polarized beam in our simulations. An axial superresolution of 0.66λ, 36% enhanced from the diffraction limit can be realized under the EGPG condition (pupil mask parameters: $r_1 = 0.406$; $r_2 = 0.983$; amplitude attenuation of the ring is 0.956). Figure 3(e) shows the intensity distribution of the focus in the x-z cross section, and Fig. 3(f) plots the intensity profile along z and x axis, respectively. The ratio between the z FWHM (0.66λ) and the x FWHM (0.627λ) is 1.06:1. The isotropy property of the focus is superior to the traditionally elliptical focus (with a typical aspect ratio between axial and lateral FWHM > 2:1). The maximum sidelobe intensity aside the optical axis is 64%, which is mainly contributed by the transversely polarized component. Figure 3(g) shows the pure longitudinal (i.e., z-polarized) component intensity distribution with a much cleaner background. With a special photosensitive layer prepared to be sensitive only to this longitudinal field component, the strong transversely polarized sidelobes can be suppressed [33–35]. On the other hand, the influence of the strong sidelobe distant from the focus center could be conceivably eliminated to some extent by using confocal configuration, or by multiphoton absorption and threshold effect.
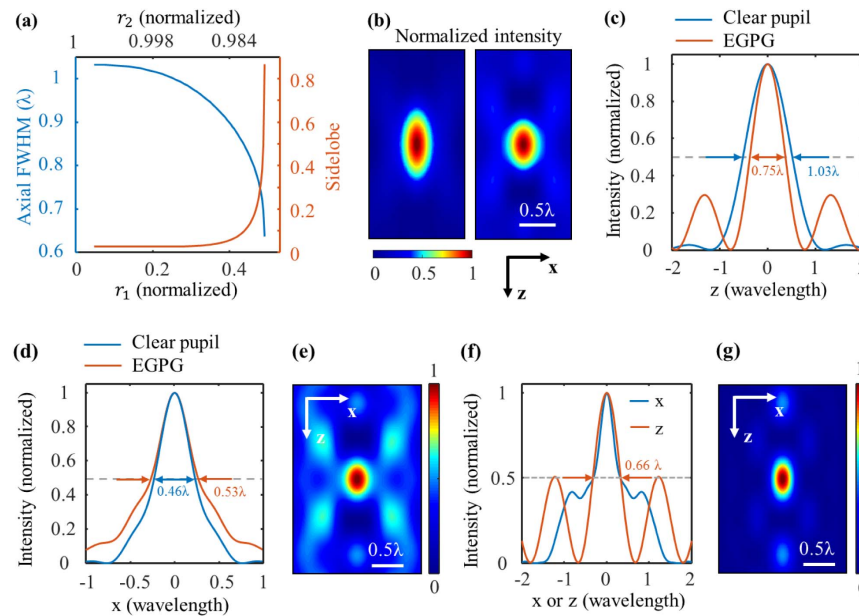
Fig. 3. (a) Axial FWHM and sidelobe of the radially polarized beam focus with the shaded-ring pupil mask whose parameters are calculated based on EGPG; energy transmittance of the mask: 30%; (b)–(d) 2D intensity distribution in x-z cross section (b), normalized intensity profile along z axis (c), and normalized intensity profile along x axis (d) of the unmodulated and the modulated focus; sidelobe intensity, 30%; (e)–(g) total intensity distribution (e), normalized intensity profile along x and z axes (f), and intensity distribution of the longitudinal component (g) of a quasi-spherical focus.

3. EXPERIMENTS

In the experiment, we utilize a phase spatial light modulator (SLM) (HED6010-NIR-011-C, HOLOEYE) to achieve the amplitude-only modulation in the pupil plane. A laser (MDL-C-405-50 mW, CNI CW Laser or Coherent Chameleon Ultra II Femtosecond Laser) is first filtered and expanded by an assembly of a lens ($f = 30$ mm), a pinhole (10 μm in diameter, P10D, Thorlabs), and another lens ($f = 150$ mm) to obtain a collimated laser beam. The polarization direction of the beam is 45° with respect to the orientation of the liquid crystal in the SLM. The phase on the SLM is set to 0 or π. The polarization direction of the beam is rotated by 90° in the π region. By adjusting the angle of a polarizer after the SLM, the ratio between the amplitude of the regions corresponding to the 0 and π phase on the SLM can be modulated to achieve the simulated shaded-ring mask, as illustrated in Figs. 4(a) and 4(b). A radial polarization converter (RADPOL4L, ARCoptix) is utilized to generate the radially polarized beam. The beam is tightly focused by a 1.4 NA oil-immersed objective (UPlanSApo, 100 × /1.40 Oil, Olympus). An Au nanoparticle (80 nm or 150 nm in diameter) on a 3D nanometer-precision motorized positioning system (P-563.3CD, PI) is used as a point object to measure the intensity distribution of the modulated focus. The scattered light is collected by a multimode fiber in a confocal configuration connected with an avalanche photodiode (APD) (SPCM-AQRH-13-FC, EXCELITAS) and the wide-field images are captured by a CCD camera (MER-130-30UM, Daheng Optics). The overall view of the experimental setup can be found in Fig. 8 in Appendix D.

To show the applicability of this mask design method on various polarization beams, the experiments have been implemented for two types of CW laser beams of radial and linear polarization, and the experimental results turn out to be very close to the simulation results. The shaded-ring
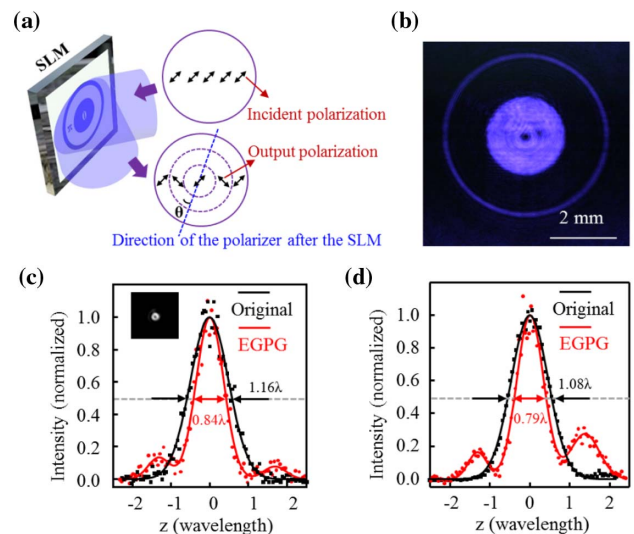

Fig. 4. Experiment on the axially superresolved focusing based on the GPG tuning. (a) Schematic diagram of converting the phase modulation to polarization direction modulation. The amplitude modulation can then be realized by adjusting the direction of polarizer after the SLM. (b) Image of the intensity distribution in the pupil plane; (c), (d) measured z profile of the focus of the (c) radially polarized beam and the (d) linearly polarized beam, respectively, with EGPG condition-based modulated pupil and unmodulated pupil. Inset in (c) is the wide-field image of an 80-nm-diameter Au nanoparticle at the focal point of the radially polarized beam.

mask with parameters corresponding to the simulations in Figs. 3(b) and 3(c) have been realized by our experimental setup ($r_1 = 0.479$, $r_2 = 0.972$, and the amplitude attenuation of the ring is 0.855). The intensity distribution in the pupil plane is shown in Fig. 4(b). Figure 4(c) shows a measured focus intensity profile of a radially polarized beam (the raw data are in supplementary Data File 1). As only z polarization exists at the focal point, the wide-field microscopy image of the Au nanoparticle located at the focal point is donut-shaped [inset in Fig. 4(c)]. When the Au nanoparticle is moving along the z axis, the scattered light intensity detected by the APD can be used to plot the profile of the focus. Due to the large diameter of the multimode fiber, the scattered light intensity would not be suppressed when the Au nanoparticle is slightly out of focus, and thus the detected FWHM of the central lobe can reflect the real condition. The profile was measured 23 times to make an average, and the averaged axial FWHM is 0.84λ, presenting an improvement by a factor of 27.6% over the 1.16λ-axial-FWHM of the conventional focus and 11.5% over the 0.95λ-axial-FWHM reported in previous work [25]. The measured intensity of sidelobes is lower than that in our simulation because of their severe defocus. Figure 4(d) shows a measured intensity profile with linearly polarized beam ($r_1 = 0.3244$ and $r_2 = 0.9616$; amplitude attenuation of the ring, 0.846; simulated sidelobe intensity, 30%; power transmittance, 20%; the raw data are in supplementary Data File 2). The average axial FWHM of profiles that were measured 10 times is 0.79λ, 26.9% finer compared with the 1.08-λ-axial-FWHM of the conventional focus. We also performed an experiment with a linearly polarized femtosecond laser and achieved 18% finer axial resolution and slightly degraded lateral resolution. The measured intensity in the x-z cross section and the plotted profiles are presented in Fig. 9 in Appendix E (the raw data are in supplementary Data File 3 and Data File 4). The focus with isotropic resolution shown in the simulation in Fig. 3(d) has not been achieved in our experiment because the attenuation contrast based on the SLM is not high enough. Using a plate fabricated with designed attenuation coating might be a solution, which can be integrated with the objective in a more compact configuration for future applications.

4. APPLICATION OF EGPG METHOD ON DIFFERENT TYPES OF PUPIL FUNCTION

(1) Using the EGPG method to design a dual-ring-shaded pupil mask, the sidelobe can be further suppressed compared to its counterpart with the single-ring-shaded pupil mask [Figs. 7(a) and 7(b) in Appendix C]. In addition, the energy residing in the sidelobes can be precisely redistributed as per demands from specific applications by reconfiguring the parameters of the dual-ring-shaded mask. For example, as shown in Fig. 7(c) in Appendix C, the energy in the first sidelobe can be shifted to the second sidelobe, away from the central peak, which may further improve the axial discernibility in some microscopy systems owing to more severe defocusing for the sidelobes.

(2) Using the EGPG method to design a π-phase ring mask [Fig. 5(a)], we can achieve a focus towards extremely high axial resolution of the main lobe. Compared with the shaded-ring
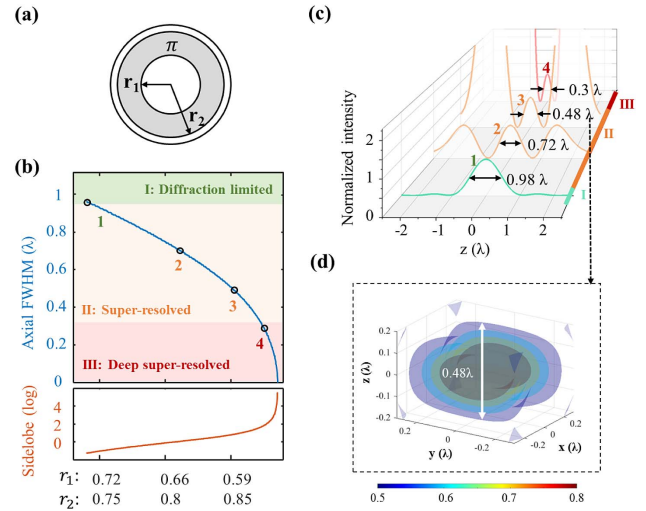

Fig. 5. Application of the EGPG method on a π phase mask. (a) Schematic of the π phase mask; (b) axial FWHM and sidelobe of an x linearly polarized beam focus modulated by the π phase ring pupil mask; (c) axial intensity profile of the foci 1–4 labeled by circles in (b). The FWHMs are shown in the figure. The axial FWHM of focus 3 is half-shortened from the diffraction limit. (d) The 3D isosurface view of focus 3; NA of the objective, 1.4; refractive index, 1.514.

pupil mask, the amplitude of the inverse focus is increased in a π-phase ring mask; thus the axial resolution can be tuned to an extreme level, but with a higher sidelobe intensity. Figure 5(b) shows that the axial FWHM of a phase mask-modulated linearly polarized focus can be decreased unlimitedly at a cost of the simultaneously increased sidelobe intensity for different ring radii, which suggests a superoscillation-like axially focusing behavior [29,30]. Figure 5(c) plots the axial intensity profile of foci 1 to 4 labeled by circles in Fig. 5(b) to show the modulation of the focal depth in detail. Their transient electric field (the real part of the calculated complex amplitude based on Debye theory) and the local wavenumber distribution (changing rate of the phase) are shown in Fig. 10 in Appendix F. The period of the oscillations around the focus center decreases gradually, and the local wavenumber becomes larger and more localized, from focus 1 to focus 4.

We categorize axial focusing behaviors via the EGPG method into three zones: I, diffraction limited; II, superresolved; and III, deep superresolved, depending on whether the axial FWHM of the main lobe is finer than the axial diffraction limit (Zone I → Zone II) or the limit of the lateral resolution with a uniform illumination, i.e., half of the media wavelength (Zone II → Zone III). Although the infinitesimal main lobe is possible in Zone III, the cost is the exponentially increased sidelobe intensity, similar to the lateral resolution modulation by superoscillation in an extreme case. For practical applications, a better trade-off is gained in Zone II. Figure 5(d) presents the 3D intensity isosurface distribution of focus 3 in Zone II, in which the axial FWHM is shortened by half from the diffraction limit. Its 2D x-z and x-y cross section intensity distribution

can be found in Fig. 11 in Appendix G. The lateral resolution is anisotropic in such a modulated linearly polarized tight-focus model. The axial sidelobe intensity is 7.65 times that of the main lobe, while the influence of the sidelobe may be conceivably minimized when the focus is utilized to deterministically manipulate the thickness of ultrathin 2D nanomaterials and fabricate functional integrated flat optoelectronic devices [36]. The vector property distribution of a deep superresolved focus with an ultrasmall FWHM of 0.1λ and accompanied by ultralarge sidelobes is presented in Fig. 12 in Appendix H to show the extremity of the modulation from a conceptual perspective. More details about the applications of the EGPG method to design a π phase mask to modulate a radially polarized beam (with laterally isotropic focus shape) can be found in Fig. 13 in Appendix I.

5. CONCLUSION AND OUTLOOK

In conclusion, we have proposed a GPG tuning-based method with an interference model for axial superresolved focusing via beam modulation in the pupil, which possesses the merits of compact configuration and general applicability on the existing (superresolved or traditional) microscope system such as the confocal or the two-photon systems to upgrade their axial resolution. The pupil mask is decomposed to a clear pupil and an inverse mask, and the optimal axial resolution can be attained by utilizing the completely destructive interference between the two corresponding foci. The axial resolution of a shaded-ring mask modulated radially polarized beam can be 27% improved from the diffraction limit and 11% improved from the previous resolution record. A quasi-spherical focus with an aspect ratio of 1:1:1.06 for x, y, and z FWHMs has been demonstrated in simulation, showing the potential to achieve the isotropic resolution using a simple single-objective configuration. Moreover, a superoscillation-like behavior has been observed in the axial dimension with the conceptual possibility toward extremely high axial resolution. The method has been proved to be efficient for multiple types of polarizations and pupil masks. By introducing more rings in the pupil mask, the sidelobe intensity distribution could be manipulated for adaptation to specific applications. In the future, the SLM could be substituted by a plate fabricated using photolithography and film coating techniques, to improve the axial resolution of a microscope system simply by inserting the thin plate in the pupil plane of the objective. The costs of the implementation include lowered focusing efficiency, slightly degraded lateral resolution, and increased sidelobe intensity, which could be overcome by increasing the source energy, introducing more modulation freedoms, and using an optical system that can suppress the defocused energy. The specific applications that can be explored in the future may include the 3D omnidirectionally superresolved microscopy with a confocal system, and the omnidirectional laser direct writing of a circular waveguide by combining the threshold effect of the photoresist, so as to suppress the strong sidelobes, and so forth. In a word, the research may benefit a wide spectrum of applications, such as 3D laser fabrication, superresolution imaging, and light trapping, which increasingly require axial superresolved and isotropic focusing properties.

APPENDIX A: DEDUCTION OF THE GOUY PHASE GRADIENT OF THE INVERSE FOCUS

Considering the vector focusing theory, the complex field along the optical axis of the inverse focus can be written as Eq. (A1),

$$\boldsymbol{E}_{\mathrm{inv}} \propto \int_{\theta_1}^{\theta_2} [\boldsymbol{x} \cdot A_x(\Theta) + \boldsymbol{y} \cdot A_y(\Theta) + \boldsymbol{z} \cdot A_z(\Theta)]$$
$$\times e^{i \cdot (n \cdot k \cdot z \cdot \cos \Theta + \pi)} \mathrm{d}\Theta, \tag{A1}$$

where θ_1 and θ_2 denote the minimum and maximum convergence angles of the transmitted beam, as shown in Fig. 2(a). Θ is the convergence angle; $A_{x,y,z}(\Theta)$ denote the amplitude contribution to the x-, y-, or z-polarized focus field by a light beam with uniform intensity distribution in the pupil plane at the convergence angle Θ. For a radially polarized beam, only z-polarized components exist along the optical axis: $A_z(\Theta) = \sqrt{\cos \Theta} \sin^2 \Theta$ and $A_{x,y}(\Theta) = 0$. For linearly or circularly polarized beam, the polarization state along the optical axis is the same as the polarization state of the incident beam. For the x linearly polarized beam, $A_x(\Theta) = \sqrt{\cos \Theta} \sin \Theta (1 + \cos \Theta)$ and $A_{y,z}(\Theta) = 0$.

We simplify Eqs. (A1) and (A2), in which only the axial dominate polarization of the focus is considered, i.e., z polarization for the radially polarized incident beam and x polarization for the x linearly polarized incident beam,

$$E_{\mathrm{inv}} \propto \int_{\theta_1}^{\theta_2} A(\Theta) e^{i \cdot (n \cdot k \cdot z \cdot \cos \Theta + \pi)} \mathrm{d}\Theta. \tag{A2}$$

In the vicinity of the focus center, $z \approx 0$, and $e^{i \cdot n \cdot k \cdot z \cdot \cos \Theta}$ can be approximated to $1 + i \cdot n \cdot k \cdot z \cdot \cos \Theta$. So we have Eq. (A3),

$$E_{\mathrm{inv}} \propto \int_{\theta_1}^{\theta_2} -A(\Theta) \mathrm{d}\Theta + i \cdot \int_{\theta_1}^{\theta_2} -A(\Theta) \cdot n \cdot k \cdot z \cdot \cos(\Theta) \mathrm{d}\Theta. \tag{A3}$$

The Gouy phase of the inverse focus can be calculated by Eq. (A4),

$$\mathrm{GP}_{\mathrm{inv}} = \arctan\left[\frac{\int_{\theta_1}^{\theta_2} A(\Theta) \cdot n \cdot k \cdot z \cdot \cos(\Theta) \mathrm{d}\Theta}{\int_{\theta_1}^{\theta_2} A(\Theta) \mathrm{d}\Theta}\right] - n \cdot k \cdot z. \tag{A4}$$

The GPG of the inverse focus can be calculated by Eq. (A5),

$$\left.\frac{\mathrm{d}(\mathrm{GP}_{\mathrm{inv}})}{\mathrm{d}z}\right|_{z=0} = \frac{\mathrm{d}[\int_{\theta_1}^{\theta_2} A(\Theta) \cdot n \cdot k \cdot z \cdot \cos \Theta \mathrm{d}\Theta / \int_{\theta_1}^{\theta_2} A(\Theta) \mathrm{d}\Theta]}{\mathrm{d}z}$$
$$\cdot \cos^2[\mathrm{GP}_{\mathrm{inv}}(z=0)] - n \cdot k$$
$$= \int_{\theta_1}^{\theta_2} A(\Theta) \cdot n \cdot k \cdot \cos \Theta \mathrm{d}\Theta / \int_{\theta_1}^{\theta_2} A(\Theta) \mathrm{d}\Theta - n \cdot k. \tag{A5}$$

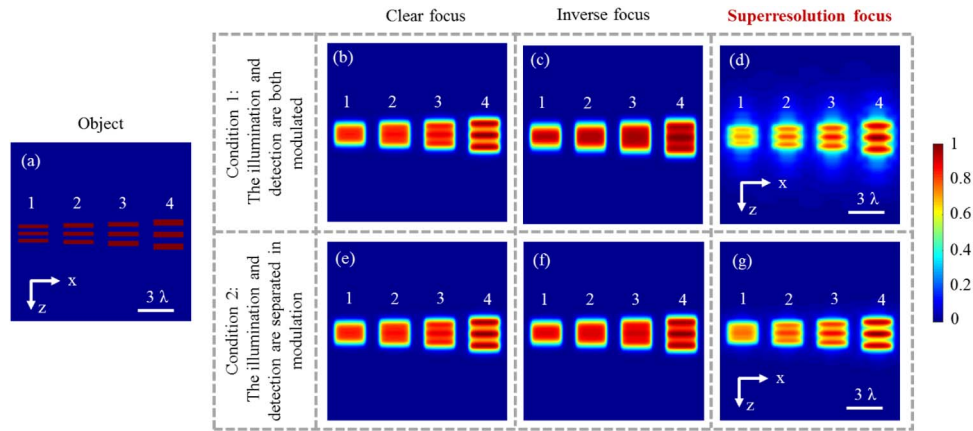## APPENDIX B: UTILIZATION OF EGPG METHOD TO UPGRADE THE AXIAL RESOLUTION OF A CONFOCAL SYSTEM

Fig. 6. Images in the x–z cross section of four objects with different periods (z denotes the direction of the optical axis). (a) Objects 1–4 with periods of 0.6λ, 0.7λ, 0.8λ, and λ, respectively; (b)–(d) images simulated considering condition 1, in which the illumination and detection are both modulated by the clear pupil, inverse pupil, and shaded-ring pupil shown in Fig. 1(a). Parameters of the shaded-ring pupil mask are the same as those demonstrated in Fig. 3(c). (e)–(g) Images simulated considering condition 2, in which only the illumination or detection is modulated; the periods of 0.6λ in (d) and 0.7λ in (g) are resolved, where the shaded-ring modulated superresolution focus is utilized. The period of 0.8λ is resolved by the original focus in (b) and (e). The axial resolution can be improved 25% in condition 1, and improved 12.5% in condition 2, while the better contrast and cleaner background are enabled in condition 2.

APPENDIX C: SIDELOBE INTENSITY SUPPRESSION AND MODULATION BY INTRODUCING MORE RINGS

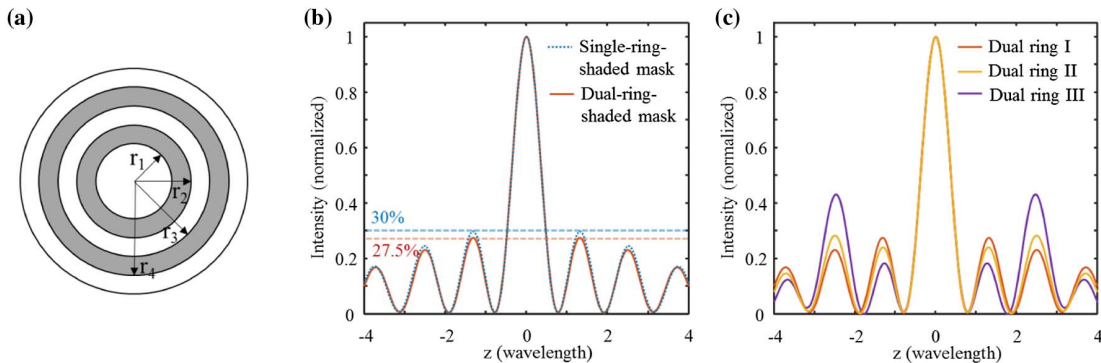## APPENDIX D: SCHEMATIC OF THE EXPERIMENTAL SETUP

Fig. 7. Normalized intensity profile along z axis of the dual-ring-shaded pupil mask modulated focus. (a) Schematic diagram of the dual-ring-shaded pupil mask; (b) two focus profiles modulated by a single-ring-shaded pupil mask and a dual-ring-shaded pupil mask, respectively. The parameters of the single-ring mask are the same as those demonstrated in Fig. 3(c). The normalized radius of the dual-ring mask: $r_{1,2,3,4} = 0.469, 0.811, 0.817,$ and 0.974, respectively, and the amplitude attenuation factor is 0.85. The maximum sidelobe intensity is lowered in the dual-ring modulated focus. (c) Focus profiles modulated by three dual-ring-shaded pupil masks, showing that the power of sidelobes is pushed further from the central peak. Dual ring I: $r_{1,2,3,4} = 0.469, 0.811, 0.817, 0.974$; amplitude attenuation, 0.85. Dual ring II: $r_{1,2,3,4} = 0.4688,$ $0.8107, 0.8188, 0.9736$; amplitude attenuation, 0.87. Dual ring III: $r_{1,2,3,4} = 0.459, 0.804, 0.826, 0.975$; amplitude attenuation, 0.92. All the foci possess the same power transmission efficiency (30%) and the same FWHM of the central peak (0.75λ). NA of the objective, 1.4; refractive index, 1.514.
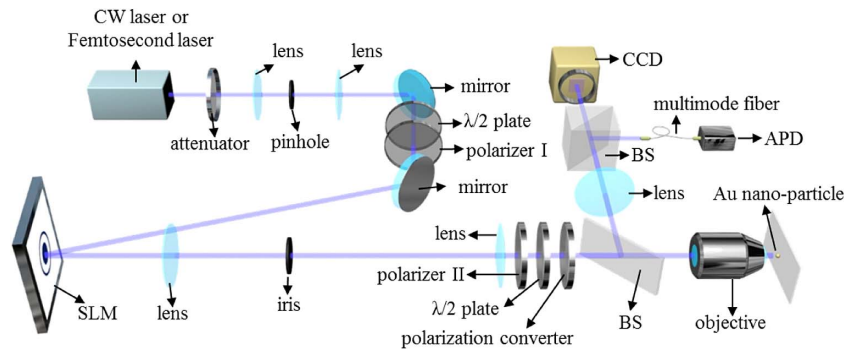
Fig. 8. Schematic of experimental setup. BS, beam splitter; SLM, spatial light modulator.

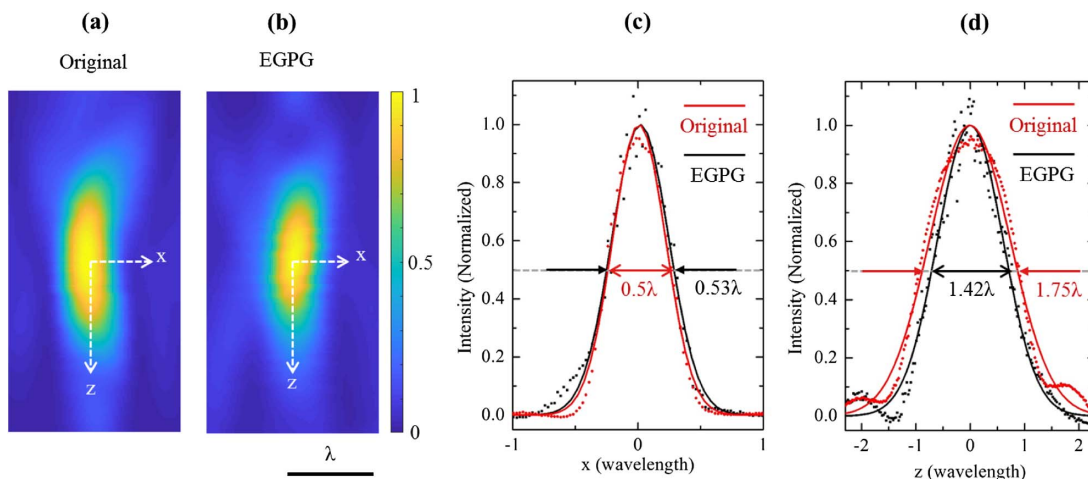## APPENDIX E: AXIAL SUPERRESOLVED FOCUS MODULATION FOR A FEMTOSECOND LASER

Fig. 9. 2D focus intensity distribution in the *x-z* cross section of a linearly polarized femtosecond laser. (a) 2D intensity distribution of the original unmodulated focus; (b) 2D intensity distribution of the shaded-ring pupil function modulated focus based on the EGPG condition; (c) lateral intensity distribution of the two foci in (a), (b); (d) axial intensity distribution of the two foci in (a), (b); the data are fitted using the Gaussian function. The axially prolonged focus might be attributed to the interaction between the femtosecond laser with the Au nanoparticle and the optical system. Laser information: central wavelength, 800 nm; pulse width, 140 fs; Coherent Chameleon Ultra II, femtosecond laser.

APPENDIX F: SUPEROSCILLATION-LIKE BEHAVIOR OF THE AXIAL RESOLUTION MODULATION BASED ON EGPG
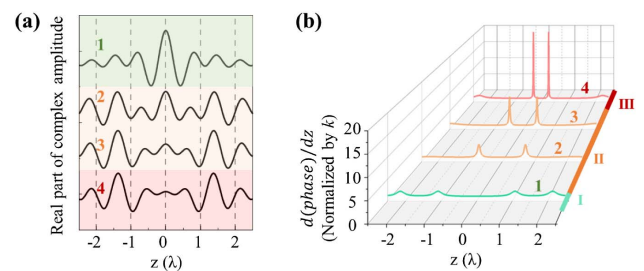

Fig. 10. (a) Transient electric field and (b) the local wave vector distribution along the *z* axis of foci 1–4 in Fig. 5(b); the transient electric field in (a) is the real part of the complex amplitude calculated based on the Debye theory. The local wave vector in (b) is the derivative of the phase of the electric field versus axial position. The derivative is much larger than the maximum wavenumber in the media. NA of the objective, 1.4; refractive index, 1.514.

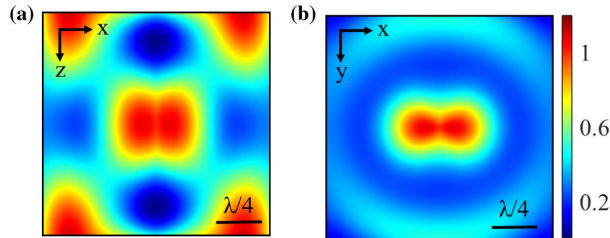## APPENDIX G: INTENSITY DISTRIBUTION OF A LINEARLY POLARIZED FOCUS WITH TWO-FOLD IMPROVED AXIAL RESOLUTION

Fig. 11. Intensity distribution in (a) x–z and (b) x–y cross section of the focus shown in Fig. 5(d).

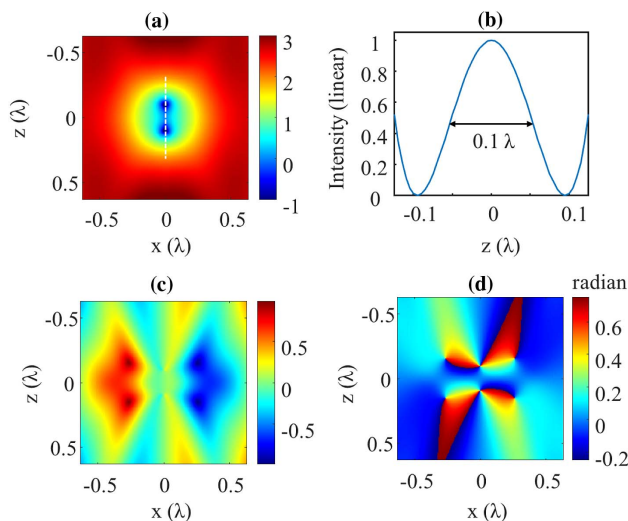## APPENDIX H: VECTOR PROPERTY OF VECTOR PROPERTY DISTRIBUTION OF A DEEP SUPERRESOLVED FOCUS WITH AN ULTRASMALL FWHM OF 0.1λ

Fig. 12. Simulation of a deep superresolved focus of linearly polarized beam with a 0.1λ ultrasmall FWHM. (a) x–z cross-sectional view of the focus; the intensity is shown in log. (b) Axial intensity profile along the white dashed line in (a); (c), (d) distribution of the polarization ellipticity and the direction of the major axis in the x–z cross section. NA of the objective, 1.4; refractive index, 1.514.

APPENDIX I: APPLICATIONS OF THE EGPG METHOD TO DESIGN A π PHASE MASK TO MODULATE A RADIALLY POLARIZED BEAM
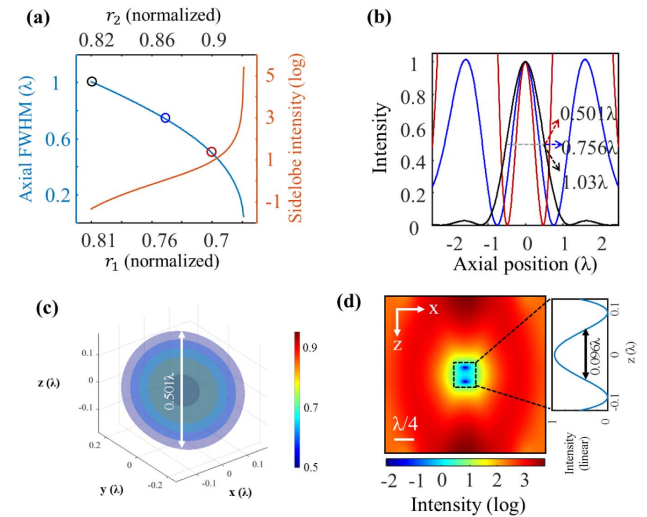

Fig. 13. Applications of the EGPG method to design a π phase mask to modulate a radially polarized beam. (a) Axial FWHM and sidelobe of a radially polarized beam focus modulated by the π phase ring pupil mask. r_1 and r_2 denote the normalized radius of the ring. (b) Axial intensity profile of the foci labeled by circles in (a) of the same color. The FWHMs are shown in the figure. (c) 3D intensity isosurface distribution of the longitudinal component of the focus, in which the axial depth is shortened by half from the diffraction limit; (d) x–z cross-sectional view of the focus with a 0.096λ ultrasmall FWHM; NA of the objective, 1.4; refractive index, 1.514.

Disclosures. The authors declare no conflicts of interest.

Data Availability. Data underlying the results presented in this paper are available in Data File 1, Data File 2, Data File 3, and Data File 4.

REFERENCES

1. D. Wei, C. Wang, H. Wang, X. Hu, D. Wei, X. Fang, Y. Zhang, D. Wu, Y. Hu, J. Li, S. Zhu, and M. Xiao, "Experimental demonstration of a three-dimensional lithium niobate nonlinear photonic crystal," Nat. Photonics **12**, 596–600 (2018).
2. G. von Freymann, A. Ledermann, M. Thiel, I. Staude, S. Essig, K. Busch, and M. Wegener, "Three-dimensional nanostructures for photonics," Adv. Funct. Mater. **20**, 1038–1052 (2010).
3. M. Deubel, G. von Freymann, M. Wegener, S. Pereira, K. Busch, and C. M. Soukoulis, "Direct laser writing of three-dimensional photonic-crystal templates for telecommunications," Nat. Mater. **3**, 444–447 (2004).
4. J. Bauer, A. Schroer, R. Schwaiger, and O. Kraft, "Approaching theoretical strength in glassy carbon nanolattices," Nat. Mater. **15**, 438–443 (2016).

5. T. Frenzel, M. Kadic, and M. Wegener, "Three-dimensional mechanical metamaterials with a twist," Science 358, 1072–1074 (2017).
6. D. Wu, Q.-D. Chen, L.-G. Niu, J.-N. Wang, J. Wang, R. Wang, H. Xia, and H.-B. Sun, "Femtosecond laser rapid prototyping of nanoshells and suspending components towards microfluidic devices," Lab Chip 9, 2391–2394 (2009).
7. Y. Liao, J. Song, E. Li, Y. Luo, Y. Shen, D. Chen, Y. Cheng, Z. Xu, K. Sugioka, and K. Midorikawa, "Rapid prototyping of three-dimensional microfluidic mixers in glass by femtosecond laser direct writing," Lab Chip 12, 746–749 (2012).
8. G. Cerullo, R. Osellame, S. Taccheo, M. Marangoni, D. Polli, R. Ramponi, P. Laporta, and S. De Silvestri, "Femtosecond micromachining of symmetric waveguides at 1.5 μm by astigmatic beam focusing," Opt. Lett. 27, 1938–1940 (2002).
9. R. Osellame, V. Maselli, R. M. Vazquez, R. Ramponi, and G. Cerullo, "Integration of optical waveguides and microfluidic channels both fabricated by femtosecond laser irradiation," Appl. Phys. Lett. 90, 231118 (2007).
10. R. M. Vazquez, R. Osellame, D. Nolli, C. Dongre, H. van den Vlekkert, R. Ramponi, M. Pollnau, and G. Cerullo, "Integration of femtosecond laser written optical waveguides in a lab-on-chip," Lab Chip 9, 91–96 (2009).
11. J. P. Hadden, V. Bharadwaj, B. Sotillo, S. Rampini, R. Osellame, J. D. Witmer, H. Jayakumar, T. T. Fernandez, A. Chiappini, C. Armellini, M. Ferrari, R. Ramponi, P. E. Barclay, and S. M. Eaton, "Integrated waveguides and deterministically positioned nitrogen vacancy centers in diamond created by femtosecond laser writing," Opt. Lett. 43, 3586–3589 (2018).
12. N. Lindenmann, G. Balthasar, D. Hillerkuss, R. Schmogrow, M. Jordan, J. Leuthold, W. Freude, and C. Koos, "Photonic wire bonding: a novel concept for chip-scale interconnects," Opt. Express 20, 17667–17677 (2012).
13. K. Wang, H. Qian, Z. Liu, and P. K. Yu, "Second-order nonlinear susceptibility enhancement in gallium nitride nanowires," Prog. Electromagn. Res. 168, 25–30 (2020).
14. S. Thiele, K. Arzenbacher, T. Gissibl, H. Giessen, and A. M. Herkommer, "3D-printed eagle eye: compound microlens system for foveated imaging," Sci. Adv. 3, e1602655 (2017).
15. T. Gissibl, S. Thiele, A. Herkommer, and H. Giessen, "Two-photon direct laser writing of ultracompact multi-lens objectives," Nat. Photonics 10, 554–560 (2016).
16. W. Chen and Q. Zhan, "Creating a spherical focal spot with spatially modulated radial polarization in 4Pi microscopy," Opt. Lett. 34, 2444–2446 (2009).
17. Q. Geng, D. Wang, P. Chen, and S.-C. Chen, "Ultrafast multi-focus 3-D nano-fabrication based on two-photon polymerization," Nat. Commun. 10, 2179 (2019).
18. S. K. Saha, D. Wang, V. H. Nguyen, Y. Chang, J. S. Oakdale, and S.-C. Chen, "Scalable submicrometer additive manufacturing," Science 366, 105–109 (2019).
19. K. I. Willig, B. Harke, R. Medda, and S. W. Hell, "STED microscopy with continuous wave beams," Nat. Methods 4, 915–918 (2007).
20. W. Liu, K. C. Toussaint, Jr., C. Okoro, D. Zhu, Y. Chen, C. Kuang, and X. Liu, "Breaking the axial diffraction limit: a guide to axial super-resolution fluorescence microscopy," Laser Photon. Rev. 12, 1700333 (2018).
21. T. J. Gould, D. Burke, J. Bewersdorf, and M. J. Booth, "Adaptive optics enables 3D STED microscopy in aberrating specimens," Opt. Express 20, 20998–21009 (2012).
22. H. Ni, Y. Wang, T. Tang, W. Yu, D. Li, M. He, R. Chen, M. Zhang, and J. Qian, "Quantum dots assisted in vivo two-photon microscopy with NIR-II emission," Photon. Res. 10, 189–196 (2022).
23. D. Denkova, M. Ploschner, M. Das, L. M. Parker, X. Zheng, Y. Lu, A. Orth, N. H. Packer, and J. A. Piper, "3D sub-diffraction imaging in a conventional confocal configuration by exploiting super-linear emitters," Nat. Commun. 10, 3695 (2019).
24. X. Ouyang, Y. Xu, M. Xian, Z. Feng, L. Zhu, Y. Cao, S. Lan, B.-O. Guan, C.-W. Qiu, M. Gu, and X. Li, "Synthetic helical dichroism for six-dimensional optical orbital angular momentum multiplexing," Nat. Photonics 15, 901–907 (2021).
25. H. Lin, B. Jia, and M. Gu, "Generation of an axially super-resolved quasi-spherical focal spot using an amplitude-modulated radially polarized beam," Opt. Lett. 36, 2471–2473 (2011).
26. M. A. A. Neil, R. Juškaitis, T. Wilson, Z. J. Laczik, and V. Sarafis, "Optimized pupil-plane filters for confocal microscope point-spread function engineering," Opt. Lett. 25, 245–247 (2000).
27. M. Martínez-Corral, C. Ibáñez-López, G. Saavedra, and M. T. Caballero, "Axial gain resolution in optical sectioning fluorescence microscopy by shaded-ring filters," Opt. Express 11, 1740–1745 (2003).
28. M. Martínez-Corral, M. T. Caballero, E. H. K. Stelzer, and J. Swoger, "Tailoring the axial shape of the point spread function using the Toraldo concept," Opt. Express 10, 98–103 (2002).
29. K. Huang, H. Ye, J. Teng, S. P. Yeo, B. Luk'yanchuk, and C.-W. Qiu, "Optimization-free superoscillatory lens using phase and amplitude masks," Laser Photon. Rev. 8, 152–157 (2014).
30. F. Qin, K. Huang, J. Wu, J. Teng, C.-W. Qiu, and M. Hong, "A supercritical lens optical label-free microscopy: sub-diffraction resolution and ultra-long working distance," Adv. Mater. 29, 1602721 (2017).
31. C. Ibáñez-López, G. Saavedra, G. Boyer, and M. Martínez-Corral, "Quasi-isotropic 3-D resolution in two-photon scanning microscopy," Opt. Express 13, 6168–6174 (2005).
32. T. Ackemann, W. Grosse-Nobis, and G. L. Lippi, "The Gouy phase shift, the average phase lag of Fourier components of Hermite–Gaussian modes and their application to resonance conditions in optical cavities," Opt. Commun. 189, 5–14 (2001).
33. R. Dorn, S. Quabis, and G. Leuchs, "Sharper focus for a radially polarized light beam," Phys. Rev. Lett. 91, 233901 (2003).
34. S. Quabis, R. Dorn, M. Eberler, O. Glöckl, and G. Leuchs, "Focusing light to a tighter spot," Opt. Commun. 179, 1–7 (2000).
35. L. Zhu, Y. Cao, Q. Chen, X. Ouyang, Y. Xu, Z. Hu, J. Qiu, and X. Li, "Near-perfect fidelity polarization-encoded multilayer optical data storage based on aligned gold nanorods," Opto-Electro. Adv. 4, 210002 (2021).
36. D. Hu, H. Li, Y. Zhu, Y. Lei, J. Han, S. Xian, J. Zheng, B.-O. Guan, Y. Cao, L. Bi, and X. Li, "Ultra-sensitive nanometric flat laser prints for binocular stereoscopic image," Nat. Commun. 12, 1154 (2021).